


Direct numerical simulation of electroconvection under a uniform magnetic field

Jinxiang Cai, Dongxiao Zhao, and Gaojin Li ^{*}

*State Key Laboratory of Ocean Engineering, Shanghai 200240, China
and School of Naval Architecture, Ocean and Civil Engineering, Shanghai Jiao Tong University,
Shanghai 200240, China*



(Received 2 August 2023; accepted 20 October 2023; published 8 November 2023)

The coupling between ion transport and fluid flow near ion-selective surfaces plays a crucial role in various electrohydrodynamic applications. Above a critical voltage threshold, electroconvective vortices emerge inside the liquid electrolyte and enhance ion transport. Applying a magnetic field modifies the ion mobility and electroconvection by inducing a Lorentz force. To investigate this phenomenon, we numerically study the electroconvection under a perpendicular magnetic field by incorporating the Lorentz force into the coupled Poisson-Nernst-Planck-Stokes equation. The magnetic field induces a cross-flow similar to a pressure-driven Poiseuille flow and completely suppresses the electroconvection when the applied voltage is slightly above the critical threshold. At a high voltage, the crossflow reduces the fluctuation of ion flux passing through the ion-selective surfaces and induces net ion flux along the flow direction. The analysis of the spatial spectra of flow kinetic energy and electric energy reveals that the magnetic field reduces the size of the flow structures.

DOI: [10.1103/PhysRevFluids.8.113701](https://doi.org/10.1103/PhysRevFluids.8.113701)

I. INTRODUCTION

The directed motion of ions in a liquid electrolyte under applied electric and magnetic fields is of great interest in many microfluidic applications, such as electrochemical reactions [1,2], chemical detection [3,4], and environmental monitoring [5]. In these examples, the buffer solutions are often electrically conductive, allowing for effective control of the flow through combined electromagnetohydrodynamic effects. The electric force, which drives the migration of cations and anions along the gradient of electric potential, can trigger the electroconvection (EC) instability in a liquid electrolyte when the applied voltage exceeds a critical threshold [6,7]. The Lorentz force, which is produced by the interaction of the electric current with the magnetic field, modifies the EC of the electrolyte by inducing a circular motion of the ions [8]. The combined effects of ion electromigration and the Lorentz forces provide an effective method to pump [9], mix [10,11] and separate chemical species [12] in a fluid. However, the influence of the Lorentz forces on EC is not yet fully understood.

Without the magnetic effect, EC has been widely investigated in previous theoretical, experimental, and numerical studies [7,13–16]. Under an electric field, ion transport across ion-selective surfaces leads to concentration polarization across the electrolyte [17]. At relatively low voltages, the bulk electrolyte maintains local electroneutrality, and near the ion-selective surfaces, it forms an electric double layer (EDL) with a typical thickness ranging from $O(0.1)$ to $O(10)$ nanometers, depending on the salt concentration. As the applied voltage increases, the strong depletion of

*gaojinli@sjtu.edu.cn

ions near the ion-selective surface leads to the formation of a micrometer-sized extended space charge layer (ESCL) outside the quasiequilibrium EDL. Meanwhile, the ion transfer rate reaches the diffusion limit, resulting in a limiting current. When the applied voltage exceeds a critical value, small perturbations within the ESCL become linearly unstable, inducing a second kind electroosmotic slip flow at the edge of the ESCL and triggering spontaneous convection inside the liquid electrolyte [13]. The EC flow can greatly increase the ion transfer rate, leading to the so-called overlimiting current. Moreover, it causes current fluctuations and enhances the mixing of the fluid.

In recent years, various strategies have been explored to control EC near ion exchange surfaces for different electrochemical applications, including desalination, energy harvesting, and sensors. These strategies encompass flow confinement [18], buoyancy stabilization [19], the use of the viscoelastic electrolyte [20,21], modification of the chemical kinetics of ion-selective surfaces [22], incorporation of insulating structures in membranes [23], and implementation of pressure-driven flow of the electrolyte [24–27]. Among these studies, pressure-driven flow of liquid electrolytes has received significant attention due to its simplicity and direct relevance to microfluidic applications. The electrohydrodynamic interaction between EC and a shear flow has been extensively studied by experiments, numerical simulations, and scaling analysis. Kwak *et al.* [28] showed that the applied voltage V and the shear velocity U jointly determine the height of the EC vortices h , causing a scaling relation of $h \sim (V^2/U)^{1/3}$. In a subsequent work, Kwak *et al.* [24] studied the sheltering effects of a pressure-driven flow of electrolytes and observed four types of flow states: 1D ion polarization without EC, EC in diffusion layer, stable EC with unidirectional vortices, and chaotic EC. They also found that a strong flow is needed to confine the EC fluctuations inside the high-shear region and to generate stable unidirectional vortices close to the boundary. Liu *et al.* [27] later found that the transition from a chaotic to steady EC state occurs when the shear flow velocity is above a critical slip velocity $u_s \sim (\delta^{-1}V^4)^{1/3}$, where δ is the double layer thickness. In electrodeposition processes, the presence of cross-flow can delay the onset of EC instabilities and suppress the growth of metal dendrites [29]. Recently, Li *et al.* [26] analyzed the effects of the imposed flow on the linear instability of the combined electroconvective and morphological perturbations. Their results show that the imposed flow can fully suppress the EC instability at a sufficiently large velocity, while it has smaller effects on the morphological instability.

In microchannels of liquid electrolytes, applying a magnetic field perpendicular to the electric field can effectively drive or modify the fluid flow by inducing the Lorentz force [8]. This phenomenon, known as the magnetohydrodynamic (MHD) effect, has been widely studied for the development of various microfluidic devices. Bau and coworkers [9] demonstrated the feasibility of using MHD effects to control individual flow branches in a microfluidic network. By applying voltage differences to specific electrode pairs, liquid flow can be directed along desired paths without the need for mechanical valves and pumps. The MHD effect is also effective in driving the microfluidic flows of ionic liquids with much higher viscosity than aqueous electrolyte [30]. Directed flow can also be generated in ac MHD micropumps using synchronized high-frequency ac current and a magnetic field generated by an electromagnet [31]. This design advantageously helps reduce electrode degradation by constantly reversing the chemical reactions inside the electrolyte solution. Das *et al.* [32] demonstrated the potential applications of MHD pumps for sample injection, low pressure chromatography, and on-chip sample analysis. Fluid stirring and mixing by MHD effects are also studied by arranging electrodes in different configurations to enhance chaotic advection [10,11,33,34]. All these studies have focused on the influence of the Lorentz force on fluid flow while neglecting the EC effects. However, considering the relatively high voltages (1–10 volts) and high ion conductivity ($10^{-2} - 1$ S/cm) in these studies, it is highly probable that EC will occur and have a significant impact on the fluid flow.

Under the constraint of electroneutrality in the electrolyte, the Lorentz body force is often irrotational and generates flows identical to those driven by a pressure gradient [35,36]. Mutschke and Bund [35] demonstrated that the simplified 2D treatment of the flow can not predict any non-trivial effect when a uniform magnetic field is perpendicular to the electric field applied to an electroneutral

fluid. Qian and Bau [36] showed that a Lorentz force potential, similar to a pressure field, can be introduced to allow the analysis of MHD flows using data from the pressure-driven flows. When an electric current is specified, this analogy can be directly applied to solve the Lorentz-force-driven flow without requiring the information about concentration and electric potential fields. While if the potential difference is the controlling variable, the full nonlinear coupling between ion transport and fluid flow must be solved. Despite the analogy, there are at least two significant differences between the Lorentz force and the pressure force. First, a Lorentz body force can induce a fluid flow in a closed conduit. This effect has been demonstrated by applying an axial magnetic field to the radial electric current to drive a fluid flow along the azimuthal direction in a circular conduit [37]. In comparison, such a flow cannot be achieved by applying a pressure gradient. Second, in the nonelectroneutral regions such as inside the ESCL, or when the magnetic field is nonuniform or has a component along the same direction as the electric field, the Lorentz force is no longer irrotational and can have unexpected impacts on the flow. Therefore, it is important to study the effects of Lorentz force in EC to fully understand the ion transport under the combined influence of magnetic and electric fields.

The influence of magnetic fields on ion transport has gained particular interest in recent years, especially for energy storage applications involving electrodeposition processes [38–40]. Magnetic fields are found to enhance the ion transport and suppress dendrite growth by altering the transport direction of the charged species and inducing extra convection of electrolytes. In zinc-air batteries, Wang *et al.* [38] investigated the interfacial behavior of zinc electrodes under the influence of a magnetic field and found it enhances the electrolyte flow by inducing rotational movement of the oxygen bubbles. This effect reduces the energy threshold for charging, suppresses dendrite growth, and extends the life cycle of zinc-air batteries. Similarly, in lithium metal batteries, the Lorentz force can effectively eliminate tip dendrite growth by causing spiral motions of lithium ions in a magnetic field [39,40]. The MHD effect reduces the fluctuation in ion transfer and promotes a more uniform and dense deposition of lithium on the electrode surface. As we will see in the following, similar effects can be observed by applying a magnetic field to EC.

Studying the EC in a magnetic field is also valuable for advancing our understanding of MHD turbulent flows in highly conducting fluids, such as liquid metals. In the high Reynolds number flow regime, a strong imposed magnetic field can largely suppress the turbulent fluctuations and delay the transition from laminar to turbulent flows [41,42]. Near an insulating wall perpendicular to the magnetic field, the formation of a thin Hartmann layer can act as an effectively slipping boundary and drive the core flow to become quasi-two-dimensional [43]. In microfluidic MHD flows, the thickness of the Hartmann layers is typically much larger than the channel width, making these studies helpful in revealing the flow dynamics inside the Hartmann layers.

In this paper, we conduct a numerical study on the influence of a magnetic field on the electrohydrodynamics of ion transport between two ion-selective surfaces. The magnetic field is applied perpendicular to a two-dimensional channel of electrolytes, where the voltage is high enough to induce EC. The rest of the paper is organized as follows: Section II discusses the governing equations and the numerical setup, Sec. III presents the results of the numerical simulation, and concluding remarks are provided in Sec. IV.

II. GOVERNING EQUATIONS AND SIMULATION SETUP

As shown in Fig. 1, we conduct a two-dimensional simulation of a binary univalent electrolyte confined between two ion-selective surfaces subjected to a voltage difference V_H . A uniform magnetic field \mathbf{B} is applied perpendicular to the potential gradient. The two-dimensional model is employed here to simulate microfluidic flows in a high-aspect-ratio channel driven by electromagnetohydrodynamic effects. Previous experiments consistently demonstrated that the EC flows are mainly two-dimensional in a channel where its thickness is an order of magnitude smaller than the height [24,28,33]. In our simulation, we neglect the induced magnetic field since the typical magnetic Reynolds number $\text{Re}_m = UH/\eta \ll 1$ for dilute electrolytes in microfluidic channels [36],

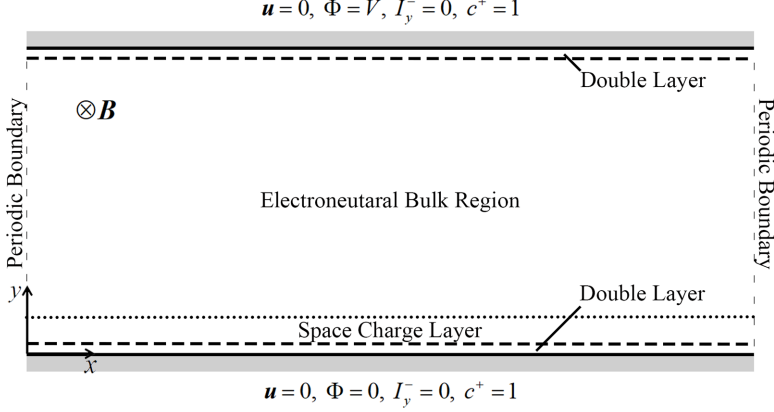


FIG. 1. Simulation setup for electroconvection (EC) between two ion-selective surfaces under a uniform magnetic field.

where U and H are the characteristic velocity and length scales, η is the magnetic diffusivity. The governing equations include the Nernst-Planck equation for ion transport, the Poisson equation for the electric potential, and the Stokes equation for the incompressible flow,

$$\frac{\partial c^\pm}{\partial t} + \nabla \cdot \mathbf{I}^\pm = 0, \quad \mathbf{I}^\pm = \mathbf{u}c^\pm - D\nabla c^\pm \mp \frac{DF}{RT}c^\pm(\nabla\Phi - \mathbf{u} \times \mathbf{B}), \quad (1a)$$

$$-\varepsilon\varepsilon_0\nabla^2\Phi = \rho, \quad \rho = F(c^+ - c^-), \quad (1b)$$

$$-\nabla p + \mu\nabla^2\mathbf{u} - \rho\nabla\Phi + \mathbf{I} \times \mathbf{B} = 0, \quad (1c)$$

$$\nabla \cdot \mathbf{u} = 0, \quad (1d)$$

where c^\pm represents the concentrations of cations and anions; \mathbf{I}^\pm is the ion flux density; including contributions from convection, diffusion, migration, and electromagnetic induction; Φ is the electric potential; \mathbf{B} is the magnetic field intensity; \mathbf{u} is the fluid velocity; p is the pressure; $\mathbf{I} = F(\mathbf{I}^+ - \mathbf{I}^-)$ is the electric current density; ρ is the charge density; μ is the fluid viscosity; $D = D^+ = D^-$ is the diffusivity for cations and anions; and ε , ε_0 , R , T , and F are the dielectric constant, vacuum permittivity, gas constant, temperature, and Faraday constant, respectively.

On the ion-selective surfaces, the boundary conditions are

$$\text{at } y = 0: \quad \mathbf{u} = 0, \quad \Phi = 0, \quad I_y^- = 0, \quad c^+ = c_0, \quad (2)$$

representing the conditions of no-slip and no-penetration conditions for fluid, the grounded electric potential, zero flux of anions, and a fixed cation concentration c_0 at the bottom surface. On the other side, the conditions are

$$\text{at } y = H: \quad \mathbf{u} = 0, \quad \Phi = V_H, \quad I_y^- = 0, \quad c^+ = c_0. \quad (3)$$

Periodic boundary conditions are used for all variables on the left and right sides of the simulation domain.

The above equations are nondimensionalized as follows: lengths by the gap distance H , velocity by $U_0 = \varepsilon\varepsilon_0(RT)^2/(F^2\mu H)$ derived by balancing the characteristic electric Maxwell stress and the viscous stress, time by H^2/D , ion concentration by c_0 , ion flux density by Dc_0/H , electric current density by FDc_0/H , potential by RT/F , pressure and stresses by $\mu U_0/H$, and magnetic field by its magnitude $|\mathbf{B}|$. The dimensionless (represented by $*$) governing equations and boundary conditions

are

$$\frac{\partial c^{\pm*}}{\partial t^*} + \nabla \cdot \mathbf{I}^{\pm*} = 0, \quad \mathbf{I}^{\pm*} = \text{Pe} \mathbf{u}^* c^{\pm*} - \nabla c^{\pm*} \mp c^{\pm*} (\nabla \Phi^* - A \mathbf{u}^* \times \mathbf{B}^*), \quad (4a)$$

$$-2\delta^2 \nabla^2 \Phi^* = \rho^*, \quad (4b)$$

$$-\nabla p^* + \nabla^2 \mathbf{u}^* + \nabla^2 \Phi^* \nabla \Phi^* + M \mathbf{I}^* \times \mathbf{B}^* = 0, \quad (4c)$$

$$\nabla \cdot \mathbf{u}^* = 0. \quad (4d)$$

$$\text{at } y = 0: \quad \mathbf{u}^* = 0, \quad \Phi^* = 0, \quad I_y^{-*} = 0, \quad c^{+*} = 1, \quad (4e)$$

$$\text{at } y = 1: \quad \mathbf{u}^* = 0, \quad \Phi^* = V = \frac{V_H F}{RT}, \quad I_y^{-*} = 0, \quad c^{+*} = 1. \quad (4f)$$

In what follows, the superscript $*$ will be dropped for brevity.

The dimensionless governing equations involve five key dimensionless parameters in this study: the Peclet number $\text{Pe} = U_0 H / D$, which describes the coupling strength between electric and hydrodynamic effects, the magnetic field strength describing the ratio of electromagnetic force to viscous force $M = DF c_0 B H / (\mu U_0)$, the normalized voltage V , the dimensionless double layer thickness $\delta = \sqrt{\varepsilon \varepsilon_0 R T / (2 F^2 c_0)} / H$, and $A = \varepsilon \varepsilon_0 |\mathbf{B}| R T / (\mu F)$, which represents the relative strength of the electromagnetic induction current compared to the applied current. For typical electrolytes, $A \sim 10^{-8}$ and therefore the induction current can be neglected [8]. In literature, the magnetohydrodynamics is typically characterized by the Hartmann number $\text{Ha} = B H \sqrt{\sigma / \mu}$, where $\sigma = DF^2 c_0 / RT$ is the electric conductivity of the solution. The Hartmann number characterizes the ratio of electromagnetic force to the viscous force using a different characteristic velocity $U'_0 = DF c_0 / \sqrt{\sigma \mu}$. For liquid electrolytes, $M / \text{Ha} = U'_0 / U_0$ is typically on the order 10^{-5} . In typical experiments, the channel width $H \sim 0.1 - 1$ mm, the fluid viscosity $\mu \sim 10^{-3}$ Pa s, conductivity $\sigma \sim 0.5$ S/cm, ion concentration $c_0 \sim 10^{-3}$ M for dilute electrolyte, ion diffusivity $D \sim 10^{-9}$ m²/s, the dielectric constant of typical electrolytes $\varepsilon \sim 1 - 10^2$, the applied voltage ranges from 0 to 2 volts, and the maximum magnetic field $|\mathbf{B}| \sim 1$ T. Based on these parameters, we estimate the values of the dimensionless parameters and choose $\text{Pe} = 0.5$, $\delta = 10^{-5} - 10^{-3}$, $V = 20 - 80$, and $M = 0 - 200$, corresponding to $\text{Ha} = 0 - 2 \times 10^{-3}$ in this paper.

The governing equations are numerically solved using a hybrid spectral-finite-volume method for a two-dimensional rectangular domain. In this method, the equations are solved in Fourier space along the x direction and in physical space in the y direction [15,20]. The domain width in the x direction is set to $L = 12$ unless otherwise specified. In the range of voltages studied, this domain size is sufficiently larger than the typical correlation length scale in the x direction [15]. More details about the numerical method can be found in Ref. [16]. The grid is uniform along the x direction and stretched in the y direction, with the grid size of $\Delta x = 5.86 \times 10^{-3}$, $\Delta y_{\min} = 1 \times 10^{-4}$, $\Delta y_{\max} = 1.576 \times 10^{-2}$, and the time step $\Delta t = 1 \times 10^{-7}$. The 1D steady ion concentration and potential profiles are used as the initial state for the simulations. The numerical validation can be found in our previous work [22].

III. RESULTS AND DISCUSSION

In this section, we will examine the influence of a uniform magnetic field on EC and ion transport. The magnetic field, which is applied perpendicular to the gradient of the electric potential, generates a Lorentz force that drives the electrolytes to flow from left to right. In the absence of EC, this flow resembles the pressure-driven flow since the Lorentz force arises from a constant current [36]. However, when the applied voltage exceeds a critical value, the emergence of EC vortices leads to a nonuniform distribution of the Lorentz force, which in turn modifies the EC. Qin and Bau [36] have shown that a uniform magnetic field perpendicular to a 2D electroneutral fluid generates an irrotational body force, which is equivalent to applying a pressure gradient. However, this equivalence no longer holds in nonelectroneutral regions. To observe this effect, we take the

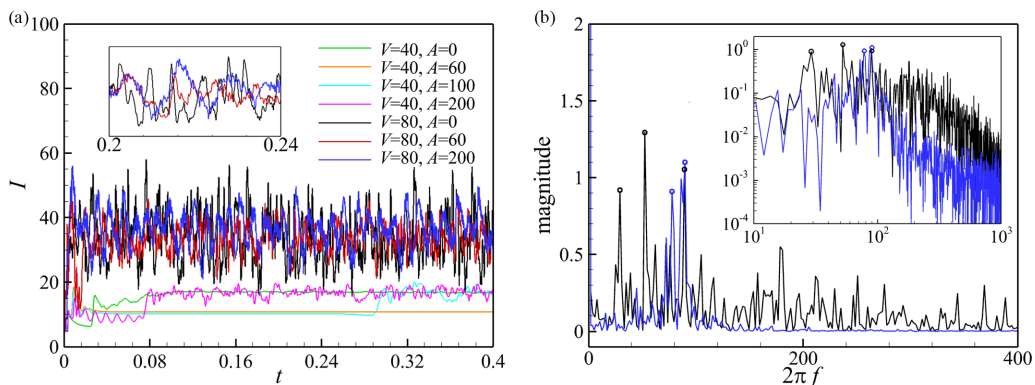


FIG. 2. (a) Time history of the x -averaged current density I under different magnetic fields for $V = 40$ and 80 . (b) Time frequency of I for $V = 80$ at (black) $M = 0$ and (blue) $M = 200$.

curl of the Lorentz force and find that

$$\nabla \times (\mathbf{I} \times \mathbf{B}) = (\mathbf{B} \cdot \nabla)\mathbf{I} + \mathbf{I}(\nabla \cdot \mathbf{B}) - (\mathbf{I} \cdot \nabla)\mathbf{B} - \mathbf{B}(\nabla \cdot \mathbf{I}) = \mathbf{B} \frac{\partial \rho}{\partial t}, \quad (5)$$

where the first three terms vanish due to the orthogonality between the magnetic field and electric current, Gauss's law for magnetism, and the constancy of the magnetic field, while the last term remains nonzero and is directly associated with the time variation of the charge density. This result suggests that the ion transport may be largely modified inside the EDL and ESCL.

We first examine the effects of the Lorentz force on the current passing through the ion-selective membranes. Figure 2(a) shows the time history of x -averaged current density $I = -\langle I_y \rangle$ under different voltages and magnetic fields, where brackets represent the spatial average over the x direction. At $V = 40$ and $M = 0$, the EC may exhibit multiple steady states with vortices of different sizes coexisting in the electrolyte, and the current density is sensitive to the dynamics of the vortices [44]. Around $t \sim 0.025$, the current nearly doubles from $I \sim 10$ to $I \sim 20$, corresponding to the coalescence of small vortices into larger ones throughout the channel. Applying a magnetic field can delay or even inhibit this process. Our results show that the coalescence time first increases with M , reaching complete suppression at approximately $M \sim 60 - 80$. As M increases further, the coalescence time decreases. It demonstrates that the magnetic field can reduce the secondary instability and regulate the ion transport. At a higher voltage $V = 80$, the magnetic field has a relatively weaker effect on the magnitude of the current. Its main influence is to change the fluctuation of the current density (see inset). Without the magnetic field, the total current is wide-banded in frequency with multiple major peaks at $f = 21.9, 52.4$, and 90.7 , and more peaks at higher frequencies [see Fig. 2(b)]. At $M = 200$, the high-frequency fluctuations at $f \gtrsim 100$ are substantially suppressed, and the current shows two peaks at $f = 77.6$ and 89.6 . This is mainly because the magnetic-induced flow controls the size of the vortices near ESCL and stabilizes the chaotic EC.

Figure 3(a) compares the time- and x -averaged current density \bar{I} at different voltages under the influence of magnetic field or pressure gradient, where the overbar denotes the time average. At a small voltage $V = 20$, the current density monotonically decreases with increasing M , and it eventually reaches the limiting current by fully suppressing the EC. This result demonstrates that a strong magnetic field can effectively stabilize the convective instability, achieving similar effects as applying a pressure gradient [26]. Since the Lorentz force is a noncontact force, it offers greater flexibility in different application scenarios; for instance, it can be used to drive a flow inside a closed annular conduit [37]. At a higher voltage $V = 80$, the average current exhibits a nonmonotonic variation with increasing the magnetic field strength. In our simulation, the EC is not fully suppressed at $V = 80$ regardless of the presence of a magnetic field or a pressure

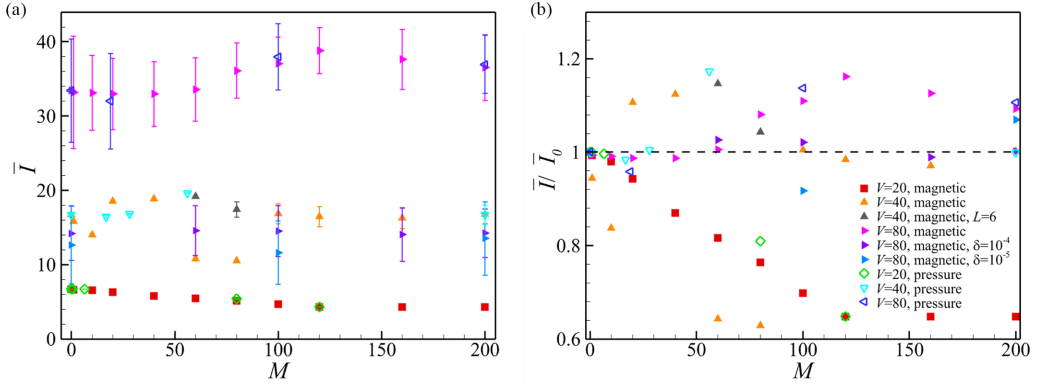


FIG. 3. (a) Time- and x -averaged current density \bar{I} versus the magnetic field strength M for different voltages. In pressure-driven cases, the equivalent magnetic field strength M is calculated from the mean body force and current density. (b) The average currents normalized by their values at $M = 0$.

gradient. However, we found that the current density fluctuation decreases (up to around 35%) with increasing magnetic intensity. Similar results are also observed for cases with thinner double layers. At $V = 80$, $\delta = 10^{-4}$, and $\delta = 10^{-5}$, the variations in the average current and current fluctuations are around 10%. At an intermediate voltage $V = 40$, the current is sensitive to the flow conditions [44]. By reducing the channel length, we found that the current density at $V = 40$ and $M = 60$ increases to $\bar{I} = 10.8$ for $L = 12$ and $\bar{I} = 19.2$ for $L = 6$, corresponding to an increment of the vortex width. This result highlights that a large computational domain is required to accurately capture the influences of crossflow on the EC at intermediate voltages. Figure 3(b) shows the average current normalized by their values at $M = 0$. The magnetic and pressure fields can reduce the current by a maximum of about 40% at $V = 20$ and increase it by a maximum of about 20% at $V = 80$. At an intermediate voltage $V = 40$, both current increase and decrease are possible, depending on the details of the EC vortices [44].

Next, we investigate the influence of the applied magnetic field on the flow structures of EC. Figure 4 shows snapshots of the fully developed flow fields at two voltages, $V = 20$ and 80, and different values of M . For better visualization, only half of the computational domain is shown in the x direction. At both voltages, the magnetic field exhibits a suppressing effect on the EC vortices

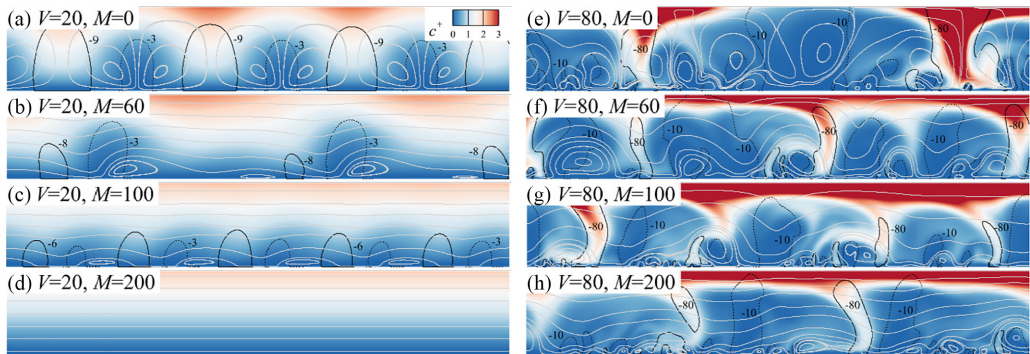


FIG. 4. Flow fields of EC at various magnetic strengths and voltages. Only half of the computational domain is displayed in the x -direction. The contour plots show the distribution of cation concentration c^+ , the black solid and dotted lines mark the regions of high and low ion fluxes, and light grey lines represent the instantaneous streamlines.

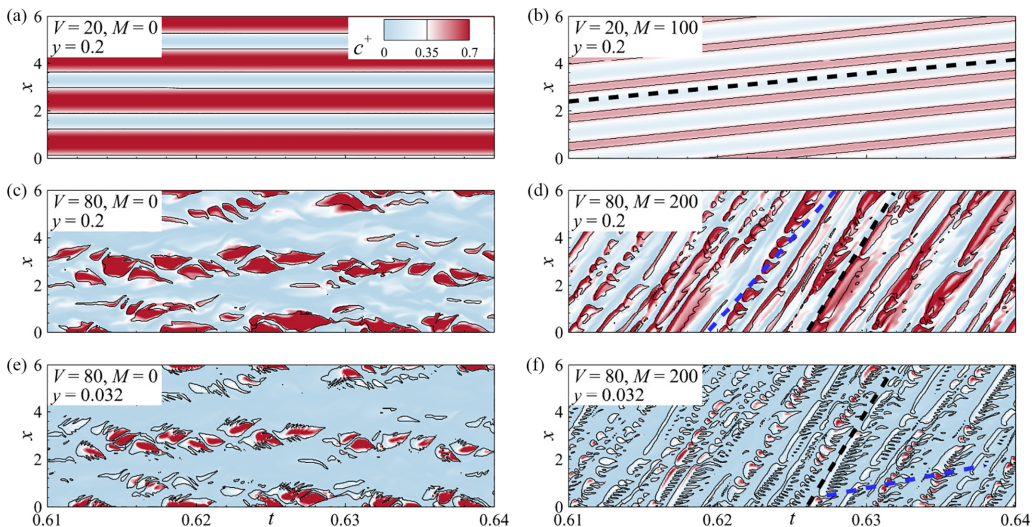


FIG. 5. Spatialtemporal evolution of the flow structures at a fixed y location for various magnetic field strengths and voltages. The contour plots show the cation concentration c^+ , the black lines mark the regions of high cation flux with $I_y^+ = -8$ for (a), (b) and $I_y^+ = -50$ for (c)–(f). The black dashed lines denote the maximum average velocity of the channel flow with (b) $\langle \bar{u} \rangle = 58$ for and (d), (f) $\langle \bar{u} \rangle = 1028$. The blue dashed lines indicate the local average velocity with (d) $\langle \bar{u} \rangle = 700$ and (f) $\langle \bar{u} \rangle = 117$.

within the bulk region, as indicated by the patterns of streamlines. At $V = 20$, the EC is steady with stationary vortex pairs filling the entire channel [Fig. 4(a)]. The aspect ratio (height/width) of the largest vortices is around 0.9, meaning the vortices are slightly wider than the gap distance between the two surfaces, consistent with previous findings [15,44]. The vortices induce upward and downward flows, directly influencing the convection of free charges. This results in alternating regions of high and low current fluxes, represented by solid and dotted black lines. The magnetic-induced crossflow suppresses the counterclockwise vortices and elongates the clockwise vortices along the flow direction. In Figs. 4(b) and 4(c), the aspect ratios of the vortices reduce to 0.3 and 0.2, respectively, causing significant reductions in the total ion flux rate near the ESCL and reducing the current variation across the channel. When M exceeds a critical threshold, the EC is completely suppressed, and the electrolyte exhibits a simple Poiseuille flow with one-dimensional ion transport cross the channel [Fig. 4(d)].

At $V = 80$, the EC becomes chaotic, with unsteady vortices continuously forming, dissipating, splitting, and merging at various length scales [Fig. 4(e)]. The ESCL experiences significant distortion due the strong electro-hydrodynamic interaction with the EC vortices, which cause substantial ejection of ions from the top surface into the bulk region. These ion injections further advect towards the bottom surface and form corridors with higher conductivity than the surrounding regions, creating local channels of extremely high ion flux rates [23]. In the absence of the magnetic field, these high-flux channels exhibit random deformation and migration across the channel. The magnetic field influences these high-flux channels in three ways: it narrows the widths of the channels, advects them along the direction of the Lorentz force, and distorts them into parabolic shapes [Figs. 4(f)–4(h)]. As we will discuss later, these three effects combined lead to a reduction in current fluctuations. Similar to the cases of $V = 20$, the magnetic-induced flow suppresses the formation of large counterclockwise vortices. Near the bottom wall, numerous small vortices are generated inside the ESCL and lead to a more uniform current distribution across the channel.

To quantitatively assess the dynamic effects of the magnetic field on EC, we analyze the spatial-temporal evolution of the flow structures at fixed y locations for different simulations. Figures 5(a)

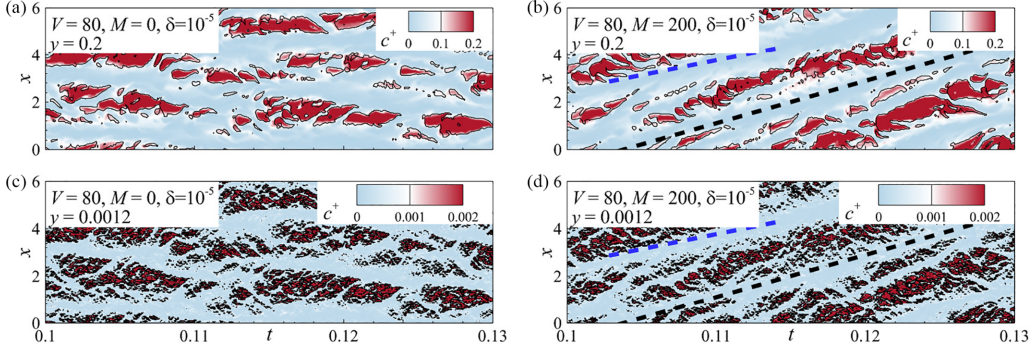


FIG. 6. Same as in Fig. 5 for $V = 80$ and $\delta = 10^{-5}$. The black dashed lines represent the maximum average velocity $\langle \bar{u} \rangle = 206$, the blue dashed lines represent the local velocities (b) $\langle \bar{u} \rangle = 128$ and (d) $\langle \bar{u} \rangle = 0.24$.

and 5(b) illustrate the results at $V = 20$ and $y = 0.2$, with magnetic field strengths of $M = 0$ and 100. Consistent with our previous findings [20], the high ion flux regions are directly associated with the high ion concentrations due to EC. At $M = 100$, the Lorentz force advects the steady vortex pairs at a constant velocity $\langle \bar{u} \rangle = 58$. The applied magnetic field also modifies the sizes and numbers of the flow structures. At a higher voltage $V = 80$, the flow structures become unstable [Fig. 5(c)]. Their duration times $t \sim 0.003$ are approximately determined by the eddy turnover time of EC vortices. At $y = 0.032$, the high concentration regions become smaller and exhibit finer filament structures, indicating the random emergence of small vortices moving away from both sides of the high concentration regions near the bottom surface [Fig. 5(e)]. In comparison, under the influence of the Lorentz force, the EC flow structures are consistently convected downstream. At both $y = 0.2$ and $y = 0.032$, the advection velocity $\langle \bar{u} \rangle = 1028$ of the large flow structures matches the maximum velocity of channel flow, as denoted by the two black dashed lines in Figs. 5(d) and 5(f). This suggests that the high-ion-flux channels experience a combined effect of advection and deformation by the shear flow. Fine filamentlike structures can be observed along the trailing side of the high-ion-flux regions, particularly at $y = 0.032$. This represents the quasiperiodic separation of small vortices from the large flow structures, which then advect downstream at a local flow velocity $\langle \bar{u} \rangle = 117$ at $y = 0.032$ (blue dashed lines). In Fig. 6, EC with thinner double layer thickness $\delta = 10^{-5}$ generates smaller vortex structures near the ESCL. These small vortices form clusters and collectively migrate downstream with the maximum flow velocity.

Figure 7(a) illustrates the normalized average velocity distribution $\langle \bar{u} \rangle / U_{\text{the}}$ over the channel, where $U_{\text{the}} = F_x / 8$ represents the maximum velocity of the theoretical Poiseuille flow $u_{\text{the}} = F_x (y - y^2) / 2$, where $F_x = MIB$ and $F_x = -dp/dx$ for a flow driven by magnetic field or pressure gradient, respectively. To enable a direct comparison, the pressure gradient is set to $-dp/dx = 433$ for $V = 20$ and $-dp/dx = 1016$ for $V = 80$, matching the average body force of the magnetic field. Interestingly, the two cases exhibit almost identical profiles for the time-averaged velocity, indicating that the key influence of the Lorentz force on EC occurs in the electroneutral bulk region. At $V = 20$, the velocity profile is exactly the same as the Poiseuille velocity, suggesting that the EC is weak compared to the crossflow. However, at a higher voltage $V = 80$, the velocity is larger in the bulk region and the maximum velocity slightly shifts towards the bottom side of the channel due to the persistence of small clockwise vortices near the bottom surface. While these vortices do not alter the linear shear flow for $y < 0.03$, they increase the fluid velocity in the bulk region (see inset). This phenomenon is caused by an electric force near the ESCL due to the fluctuation of ion concentration and electric potential. Figure 7(b) shows the dependence of the maximum flow velocity on the magnitude of the applied body force F_x . The maximum average velocity of the transverse flow under strong EC effects is $\langle \bar{U} \rangle \simeq 1.1 U_{\text{the}}$. The Lorentz force and the pressure gradient have no essential difference in driving the crossflow. We also compare our results with

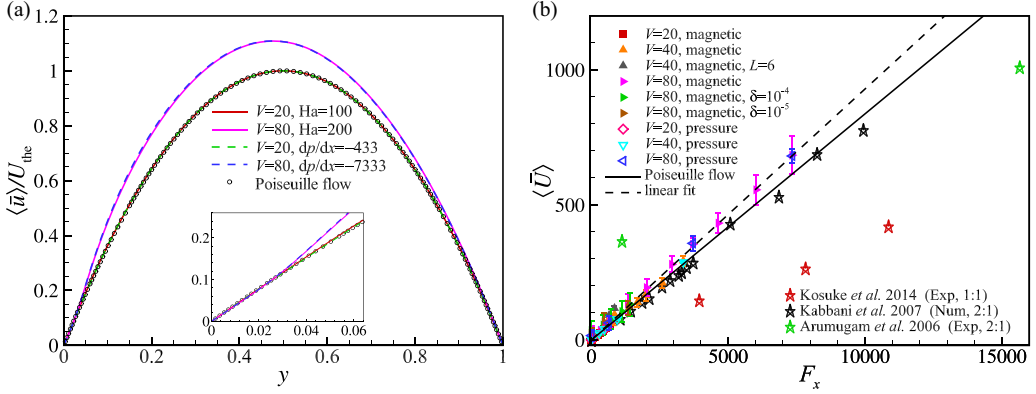


FIG. 7. (a) The time- and x -averaged flow velocity $\langle \bar{u} \rangle / U_{\text{the}}$ verse the wall normal distance y , U_{the} is the theoretical maximum velocity of the equivalent Poiseuille flow. (b) The dependence of the maximum flow velocity $\langle \bar{U} \rangle$ on the average magnitude of the driving force F_x .

previous simulations and experiments of electromagnetically driven flows [2,45,46]. It is seen that our simulation results exhibit a reasonably close agreement with the mean flow velocities reported in literature, particularly for channels with a relatively large aspect ratio of 2:1.

The transverse flow across the channel has an unexpected influence on the horizontal current flux density I_x . Figure 8 shows the distribution of I_x inside the channel at the same time instants as Fig. 4, the vectors show the current field, and the solid and dashed lines show regions of high and low current fluxes I_y . At $V = 20$, the current field exhibits a periodic variation due to the distribution of steady vortices inside the channel. At $V = 80$, these vortices induce strong downward flows, generating extremely high current flux compared to other regions. In the absence of the magnetic field, the current lines in high current regions contract at the top surface and expand near the bottom surface, and the opposite occurs in the low current regions. This is because the downward flows increase the local electric conductivity by transporting more ions from the top surface to the lower half of the channel, thereby attracting more electric field lines towards these regions. In Figs. 8(b) and 8(d), the shear flow transforms the high conductivity regions into stripe bands with parabolic shapes and significantly modifies the distribution of I_x .

On time average, the horizontal current flux \bar{I}_x should vanish at $M = 0$ with sufficient sampling. However, at $M = 200$, the crossflow induces net positive and negative current fluxes, respectively, at the upper and lower halves of the channel [see Fig. 9(b)]. To better understand this result, we decompose the average flux $\langle \bar{I}_x \rangle$ into three components: the diffusive flux $-\langle \partial_x (c^+ - c^-) \rangle$ which vanishes, the electromigration flux $-\langle (c^+ + c^-) \partial_x \Phi \rangle$, and the convective flux $\text{Pe} \langle u(c^+ - c^-) \rangle$. We find that the electromigration flux has a dominant contribution in the bulk fluid region, while the convective flux has a stronger effect near the ESCL. Further decomposition of the fluxes

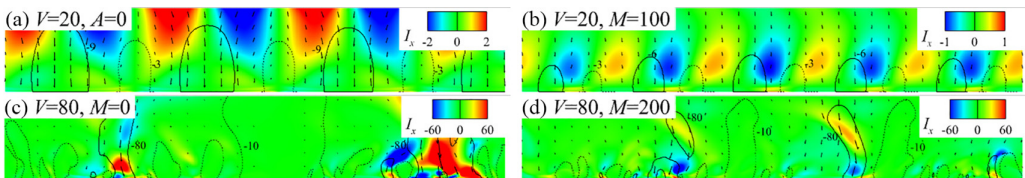


FIG. 8. Distribution of horizontal current density I_x (contour plot) at different voltages and magnetic field strengths M . The vectors represent the current field, and solid and dashed lines show the regions of high and low current densities I_y in the vertical direction.

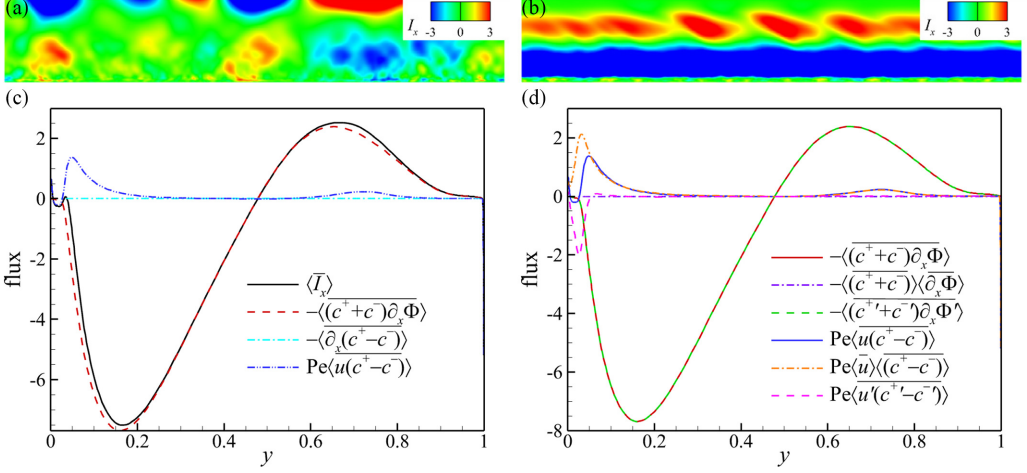


FIG. 9. The time-averaged horizontal current density \bar{I}_x fields for (a) $V = 80, M = 0$ and (b) $V = 80, M = 200$. (c), (d) Components of the average horizontal current flux $\langle \bar{I}_x \rangle$ due to advection and electromigration for $V = 80$ and $M = 200$.

demonstrates that the net horizontal flux is mainly caused by the spatial correlation between the fluctuations of salt concentration and electric potential.

The influence of the magnetic field on the ion transport can be clearly visualized in the plot of the joint probability density function (JPDF) of the two current flux components. Figure 10 shows the JPDF of I_x and I_y in the region of $0.017 \leq y \leq 0.042$, corresponding to the ESCL. For steady EC at $V = 20$, the magnetic field reduces the range of both I_x and I_y and causes a biased distribution of negative I_x . At a high voltage $V = 80$, the magnetic field significantly suppresses the intermittent events of extremely high current density ($I_y < -200$).

To analyze the influence of the Lorentz force on the length scales of the flow structures, we compute the spatial spectra for various fields by averaging the squared summation of the Fourier transformation of the vector fields' x and y components. The results are presented in both linear-log and log-log scales to provide a more comprehensive understanding. Figure 11(a) compares the spatial spectra of kinetic energy at $V = 80$ for different y locations. For both cases at $M = 0$ and $M = 200$, the kinetic energy is characterized by a power-law decay than by the exponential decay. In the region near the ESCL, a power law approximately following $E \sim k^{-5/3}$ emerges at intermediate wave numbers $k \lesssim 50$, and $E \sim k^{-8}$ at large wave numbers. The magnetic field reduces the kinetic energy distribution for $k \lesssim 3$ while enhancing the flow structures at $k \sim 50$, showing that magnetic field induces more smaller structures in the velocity field near the bottom surface, confirming the observations in Fig. 4. In the bulk region, the power-law regions are less visible, where the kinetic energy decays fast with the wave number due to the coalescence of the small vortices into larger ones. The magnetic field decreases the strength of the EC vortices while not affecting their scalings.

We further examine spectra of quantities related to the electric energy dissipation. The detailed derivation for the energy-balancing equation can be found in the work of Druzgalski *et al.* [15]. Here, we only summarize the key results. The average input power per unit width of the channel is

$$P_{\text{in}} = IV, \quad (6)$$

where $I = -\langle \bar{I}_y \rangle$ is the average current density, V is the applied voltage. The energy loss $P_{\text{loss}} = P_{\text{in}}$ in the electrolyte is composed of three parts,

$$P_{\text{loss}} = P_{\text{elec}} + P_{\text{visc}} + P_{\text{mag}}, \quad (7)$$

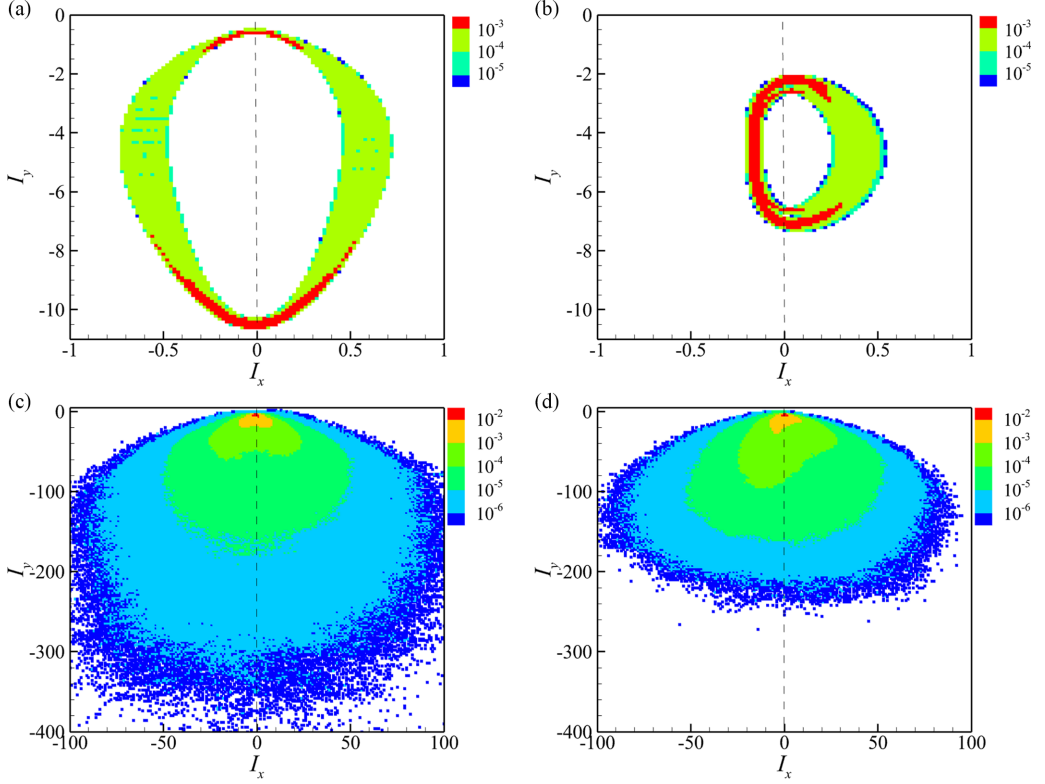


FIG. 10. Joint probability density function distributions of horizontal component I_x and vertical component I_y of current density in ESCL for $V = 20$ at (a) $M = 0$, (b) $M = 100$ and $V = 80$ at (c) $M = 0$, and (d) $M = 200$.

where

$$P_{\text{elec}} = \int_0^1 \langle \overline{p_{\text{elec}}} \rangle dy, \quad P_{\text{visc}} = \int_0^1 \langle \overline{p_{\text{visc}}} \rangle dy, \quad P_{\text{mag}} = \int_0^1 \langle \overline{p_{\text{mag}}} \rangle dy, \quad (8a)$$

$$p_{\text{elec}} = c(\nabla\Phi)^2 + \nabla\Phi \cdot \nabla\rho, \quad p_{\text{visc}} = 2\text{Pe}\delta^2(\nabla\mathbf{u})^2, \quad p_{\text{mag}} = -2\text{Pe}\delta^2\mathbf{Mu} \cdot (\mathbf{I} \times \mathbf{B}). \quad (8b)$$

The first term P_{elec} represents the electrical dissipation, which contains an Ohmic loss term and an unconventional term $\nabla\Phi \cdot \nabla\rho$ related to flux of free ions; $c = c^+ + c^-$ is the dimensionless conductivity of the electrolyte. The second and third terms are viscous dissipation and magnetic dissipation, which are both three to four orders of magnitude smaller than the electrical dissipation. The magnetic dissipation arises from the misalignment between fluid velocity and current flux and is proportional to the strength of the applied magnetic field. The electrical dissipation can also be expressed as follows:

$$p_{\text{elec}} = \frac{1}{c}[\mathbf{I} \cdot \mathbf{I} + \text{Pe}^2 \rho^2 \mathbf{u} \cdot \mathbf{u} - (\nabla\rho)^2 - 2\text{Pe}\rho \mathbf{I} \cdot \mathbf{u}] - \nabla\Phi \cdot \nabla\rho, \quad (9)$$

where the conductivity appears in the denominator of the expression.

Figures 11(b)–11(d) illustrate the spectra for $\mathbf{I} \cdot \mathbf{I}$, $\nabla\Phi \cdot \nabla\Phi$ and $\nabla\rho \cdot \nabla\rho$, where the exponential decaying characteristics is more prominent than the kinetic energy. The power spectrum of the current shows the scaling of $\sim \exp(-0.052k)$ at small wave numbers and a power-law $\sim k^{-8}$ at large wave numbers. This result is consistent with the previous experiment by Malraison and Atten [47], who studied the power spectra of current for a dielectric liquid with a space-limited

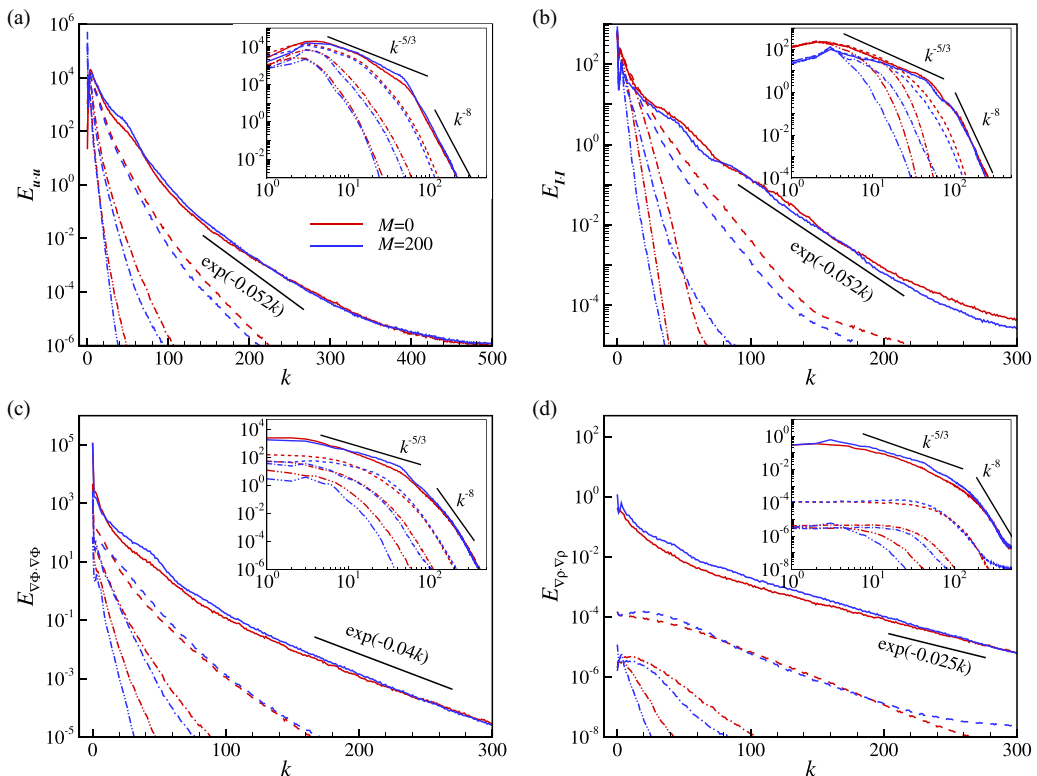


FIG. 11. Spatial spectra of (a) kinetic energy, (b) current density, (c) Ohmic loss, and (d) concentration gradient potential for $V = 80$ at $y = 0.033$ (solid lines), $y = 0.154$ (dashed lines), $y = 0.5$ (dash-dot lines), and $y = 0.806$ (dash-double-dot lines).

injection of unipolar ions near the electrode surface and observed similar scaling dependencies on the temporal frequency: exponential decay at low frequencies and power-law decay with a power exponent $\sim 7.7 - 8$ at high frequencies. These two spectra have been, respectively, related to viscous and inertial dominated flows. Our results, which are limited to low Reynolds flows (the maximum Reynolds number based on the cross-flow velocity is order of 0.1), show that similar effects can be generated by pure electromagnetoconvection instability. The magnetic field reduces the power density at low wave numbers and slightly increases the wave number for the spectra peak.

IV. CONCLUDING MARKS

To summarize, we investigate the effects of a perpendicular magnetic field on the EC instabilities in a liquid electrolyte between two ion-selective surfaces. Our paper shows that the Lorentz force drives a net crossflow similar to a Poiseuille flow driven by a pressure gradient. We observe no notable difference between the flows driven by the pressure gradient and the Lorentz force, even though the Lorentz force is rotational in the ESCL. At a voltage slightly above the critical value for the onset of EC, such as $V = 20$, the current density is decreased with increasing the magnetic field strength until it fully suppresses EC, resulting in an 1D ion-transport. This effect shares a similar physical mechanism with the pressure-driven channel suppressing EC and is consistent with previous findings [26]. On the other hand, at a high voltage, strong EC cannot be fully suppressed. The flow structures advect with the maximum speed of the crossflow and small vortices near the ESCL move with the local fluid velocity, leading to the separation of small structures from the

backside of the high-ion-flux regions. The induced crossflow is stronger than the corresponding Poiseuille flow driven by a body force with the same average magnitude of the Lorentz force. Our analysis reveals that the fluctuation of ion concentration near the ESCL generates an additional body force and enhances the velocity. Furthermore, the crossflow causes a net ion flux perpendicular to the electric field and reduces the ion flux along the direction of the electric field by suppressing the emergence of extremely high ion fluxes. The spatial spectrum of the current density shows that the magnetic field tends to reduce the size of the flow structures.

Several directions can be taken in future research to overcome the limitations of this paper. First, our current study on liquid electrolytes indicates that even though the Lorentz force is rotational inside the ESCL, it mainly has indirect effects on the EC instability by causing the crossflow similar to a pressure gradient. This is probably because the Lorentz force has a small influence on the ion mobility in a liquid electrolyte with a small conductivity $\sim 1 - 10 \text{ S m}^{-1}$, where the charge density $\sim 10^{-7} - 10^{-4} \text{ mM}$ in the ESCL and ion mobility $\sim 10^{-8} - 10^{-7} \text{ m}^2 \text{V}^{-1} \text{s}^{-1}$. In comparison, the liquid metals and ionic gases have much larger conductivity $\sim 10^6 \text{ S/m}$ and ion mobility $\sim 10^{-5} - 10^{-4} \text{ m}^2 \text{V}^{-1} \text{s}^{-1}$, and the magnetic field is found to have a much larger influence on the flow instability [48]. The Lorentz force may also have stronger effects on EC in a dielectric liquid with strong ion injection, where the density of the accumulated free charges can reach high levels $\sim 10^{-1} - 1 \text{ mM}$ at elevated voltages [49]. Future investigations focusing on such systems can explore the direct impacts of magnetic fields on EC instability. Second, our two-dimensional model is limited to the EC flows in channels of high aspect ratio. While previous studies have shown that by reducing the aspect ratio of the channel, the two-dimensional EC vortices transform into helical vortex pairs, resulting in nonmonotonic increase of overlimiting current density with respect to the channel's aspect ratio [50]. Three-dimensional simulations are necessary to explore this effect. Finally, it would be intriguing to extend the current paper to simulate the influences of the applied magnetic field on the ion transport and electrodeposition on a metal surface, considering interplay between EC and the morphological evolution of an electrode surface.

ACKNOWLEDGMENT

This paper was supported by the Natural Science Foundation of China (Grant No. 12102258).

-
- [1] L. M. A. Monzon, L. Klodt, and J. M. D. Coey, Nucleation and electrochemical growth of zinc crystals on polyaniline films, *J. Phys. Chem. C* **116**, 18308 (2012).
 - [2] H. Kabbani, A. Wang, X. Luo, and S. Qian, Modeling redox-based magnetohydrodynamics in three-dimensional microfluidic channels, *Phys. Fluids* **19**, 083604 (2007).
 - [3] Y. Chen, M. Shen, Y. Zhu, and Y. Xu, A novel electromagnet-triggered pillar valve and its application in immunoassay on a centrifugal platform, *Lab. Chip.* **19**, 1728 (2019).
 - [4] B. Srinivasan, Y. Li, Y. Jing, Y. Xu, X. Yao, C. Xing, and J. Wang, A detection system based on giant magnetoresistive sensors and high-moment magnetic nanoparticles demonstrates zeptomole sensitivity: Potential for personalized medicine, *Angew. Chem. Int. Ed.* **48**, 2764 (2009).
 - [5] A. F. Demirrs, M. T. Akan, E. Poloni, and A. R. Studart, Active cargo transport with janus colloidal shuttles using electric and magnetic fields, *Soft Matter* **14**, 4741 (2018).
 - [6] I. Rubinstein, B. Zaltzman, and I. Lerman, Electroconvective instability in concentration polarization and nonequilibrium electro-osmotic slip, *Phys. Rev. E* **72**, 011505 (2005).
 - [7] S. M. Rubinstein, G. Manukyan, A. Staicu, I. Rubinstein, B. Zaltzman, R. G. H. Lammertink, F. Mugele, and M. Wessling, Direct observation of a nonequilibrium electro-osmotic instability, *Phys. Rev. Lett.* **101**, 236101 (2008).
 - [8] S. Qian and H. H. Bau, Magneto-hydrodynamics based microfluidics, *Mech. Res. Commun.* **36**, 10 (2009).

- [9] H. Bau, J. Zhu, S. Qian, and Y. Xiang, A magneto-hydrodynamically controlled fluidic network, *Sens. Actuators B* **88**, 205 (2003).
- [10] S. Qian, J. Zhu, and H. H. Bau, A stirrer for magnetohydrodynamically controlled minute fluidic networks, *Phys. Fluids* **14**, 3584 (2002).
- [11] S. Qian and H. H. Bau, Magneto-hydrodynamic stirrer for stationary and moving fluids, *Sens. Actuators B* **106**, 859 (2005).
- [12] N. Pamme, Magnetism and microfluidics, *Lab. Chip* **6**, 24 (2006).
- [13] I. Rubinstein and B. Zaltzman, Electro-osmotically induced convection at a permselective membrane, *Phys. Rev. E* **62**, 2238 (2000).
- [14] E. A. Demekhin, N. V. Nikitin, and V. S. Shelistov, Direct numerical simulation of electrokinetic instability and transition to chaotic motion, *Phys. Fluids* **25**, 122001 (2013).
- [15] C. L. Druzgalski, M. B. Andersen, and A. Mani, Direct numerical simulation of electroconvective instability and hydrodynamic chaos near an ion-selective surface, *Phys. Fluids* **25**, 110804 (2013).
- [16] C. Druzgalski, Direct numerical simulation of electroconvective chaos near an ion-selective membrane, Ph.D. thesis, Stanford University, 2016.
- [17] A. Mani and K. M. Wang, Electroconvection near electrochemical interfaces: Experiments, modeling, and computation, *Annu. Rev. Fluid Mech.* **52**, 509 (2020).
- [18] M. B. Andersen, K. M. Wang, J. Schiffbauer, and A. Mani, Confinement effects on electroconvective instability, *Electrophoresis* **38**, 702 (2017).
- [19] E. Karatay, M. B. Andersen, M. Wessling, and A. Mani, Coupling between buoyancy forces and electroconvective instability near ion-selective surfaces, *Phys. Rev. Lett.* **116**, 194501 (2016).
- [20] G. Li, L. A. Archer, and D. L. Koch, Electroconvection in a viscoelastic electrolyte, *Phys. Rev. Lett.* **122**, 124501 (2019).
- [21] A. Sharma, A. Mukherjee, A. Warren, S. Jin, G. Li, D. L. Koch, and L. A. Archer, Electroconvective flow in liquid electrolytes containing oligomer additives, *Langmuir* **39**, 92 (2023).
- [22] G. Li, A. Townsend, L. A. Archer, and D. L. Koch, Electroconvection near an ion-selective surface with Butler-Volmer kinetics, *J. Fluid Mech.* **930**, A26 (2022).
- [23] M. Seo, W. Kim, H. Lee, and S. J. Kim, Non-negligible effects of reinforcing structures inside ion exchange membrane on stabilization of electroconvective vortices, *Desalination* **538**, 115902 (2022).
- [24] R. Kwak, V. S. Pham, and J. Han, Sheltering the perturbed vortical layer of electroconvection under shear flow, *J. Fluid Mech.* **813**, 799 (2017).
- [25] W. Liu, Y. Zhou, and P. Shi, Scaling relations in shear electroconvective vortices, *Phys. Fluids* **32**, 072009 (2020).
- [26] G. Li, A. Townsend, L. A. Archer, and D. L. Koch, Suppression of electroconvective and morphological instabilities by an imposed cross flow of the electrolyte, *Phys. Rev. Fluids* **6**, 033701 (2021).
- [27] W. Liu, Y. Zhou, and P. Shi, Critical selection of shear sheltering in electroconvective flow from chaotic to steady state, *J. Fluid Mech.* **946**, A3 (2022).
- [28] R. Kwak, V. S. Pham, K. M. Lim, and J. Han, Shear flow of an electrically charged fluid by ion concentration polarization: Scaling laws for electroconvective vortices, *Phys. Rev. Lett.* **110**, 114501 (2013).
- [29] M. C. Ma, G. Li, X. Chen, L. A. Archer, and J. Wan, Suppression of dendrite growth by cross-flow in microfluidics, *Sci. Adv.* **7**, eabf6941 (2021).
- [30] J. Wan, Y. Zuo, Z. Wang, F. Yan, L. Ge, and Z. Liang, Magnetohydrodynamic microfluidic drive of ionic liquids, *J. Microelectromech. Syst.* **23**, 1463 (2014).
- [31] A. V. Lemoff and A. P. Lee, An ac magnetohydrodynamic micropump, *Sens. Actuators B* **63**, 178 (2000).
- [32] C. Das, G. Wang, and F. Payne, Some practical applications of magnetohydrodynamic pumping, *Sens. Actuators A* **201**, 43 (2013).
- [33] H. H. Bau, J. Zhong, and M. Yi, A minute magneto hydro dynamic (MHD) mixer, *Sens. Actuators B* **79**, 207 (2001).
- [34] M. Yi, S. Qian, and H. H. Bau, A magnetohydrodynamic chaotic stirrer, *J. Fluid Mech.* **468**, 153 (2002).
- [35] G. Mutschke and A. Bund, On the 3D character of the magnetohydrodynamic effect during metal electrodeposition in cuboid cells, *Electrochem. Commun.* **10**, 597 (2008).

- [36] M. Qin and H. H. Bau, When MHD-based microfluidics is equivalent to pressure-driven flow, *Microfluid. Nanofluid.* **10**, 287 (2011).
- [37] M. Qin and H. H. Bau, Magnetohydrodynamic flow of a binary electrolyte in a concentric annulus, *Phys. Fluids* **24**, 037101 (2012).
- [38] K. Wang, P. Pei, and Y. Wang, Magnetic field improving interfacial behavior of the two-electrode system, *J. Electrochem. Soc.* **164**, A3440 (2017).
- [39] K. Shen, Z. Wang, X. Bi, Y. Ying, D. Zhang, C. Jin, G. Hou, H. Cao, L. Wu, G. Zheng *et al.*, Magnetic field-suppressed lithium dendrite growth for stable lithium-metal batteries, *Adv. Energy Mater.* **9**, 1900260 (2019).
- [40] A. Wang, Q. Deng, L. Deng, X. Guan, and J. Luo, Eliminating tip dendrite growth by Lorentz force for stable lithium metal anodes, *Adv. Funct. Mater.* **29**, 1902630 (2019).
- [41] B. Knaepen and R. Moreau, Magnetohydrodynamic turbulence at low magnetic Reynolds number, *Annu. Rev. Fluid Mech.* **40**, 25 (2008).
- [42] O. Zikanov, I. Belyaev, Y. Listratov, P. Frick, N. Razuvanov, and V. Sviridov, Mixed convection in pipe and duct flows with strong magnetic fields, *Appl. Mech. Rev.* **73**, 010801 (2021).
- [43] J. Sommeria and R. Moreau, Why, how, and when, MHD turbulence becomes two-dimensional, *J. Fluid Mech.* **118**, 507 (1982).
- [44] S. M. Davidson, M. Wessling, and A. Mani, On the dynamical regimes of pattern-accelerated electroconvection, *Sci. Rep.* **6**, 22505 (2016).
- [45] P. U. Arumugam, E. S. Fakunle, E. C. Anderson, S. R. Evans, K. G. King, Z. P. Aguilar, C. S. Carter, and I. Fritsch, Characterization and pumping: Redox magnetohydrodynamics in a microfluidic channel, *J. Electrochem. Soc.* **153**, E185 (2006).
- [46] K. Ito, T. Takahashi, T. Fujino, and M. Ishikawa, Influences of channel size and operating conditions on fluid behavior in a MHD micro pump for micro total analysis system, *Int. J. Electr. Eng.* **4**, 220 (2014).
- [47] B. Malraison and P. Atten, Chaotic behavior of instability due to unipolar ion injection in a dielectric liquid, *Phys. Rev. Lett.* **49**, 723 (1982).
- [48] S. Chandrasekhar, *Hydrodynamic and Hydromagnetic Stability* (Dover Publications, New York, 1981).
- [49] J. C. Lacroix, P. Atten, and E. J. Hopfinger, Electro-convection in a dielectric liquid layer subjected to unipolar injection, *J. Fluid Mech.* **69**, 539 (1975).
- [50] S. V. Pham, H. Kwon, B. Kim, J. K. White, G. Lim, and J. Han, Helical vortex formation in three-dimensional electrochemical systems with ion-selective membranes, *Phys. Rev. E* **93**, 033114 (2016).